PERGAMON

Journal of Structural Geology 24 (2002) 651–669

JOURNAL OF STRUCTURAL GEOLOGY

www.elsevier.com/locate/jstrugeo

Early evolution of an extensional monocline by a propagating normal fault: 3D analysis from combined field study and numerical modeling

Shawn P. Willsey[a], Paul J. Umhoefer[a,*], George E. Hilley[b]

[a]*Department of Geology, Northern Arizona University, Flagstaff, AZ 86011, USA*
[b]*Department of Geology, Arizona State University, Tempe, AZ 85287, USA*

Received 14 August 2000; revised 23 February 2001; accepted 8 June 2001

Abstract

The Nopolo structure is located along the eastern margin of the Baja California peninsula and formed during the early stages (12–6 Ma) of development of the Gulf of California. The Nopolo structure is an ~15-km-long series of two NW-striking, extensional monoclines produced by the upward propagation of normal faults. Where normal faults reach the surface, the footwall contains undisturbed, gently dipping strata, whereas the hanging wall is a highly deformed zone that contains fractured and faulted steep to subvertical strata. Long, narrow grabens with moderate to steep east-dipping strata are present in the hanging wall of the main normal faults. Initial monoclinal folding over blind normal faults produced a minimum of ~300 m of structural relief. Once the faults propagated to the surface, they offset the monoclines ~20–30 m before faulting ceased. We use an elastic dislocation model to invert fault geometry from bedding orientations around the Nopolo structure. The data are best matched by a listric normal fault that soles out at ~5 km depth. The model suggests that the tip line of the fault was located ~1 km below the surface prior to the breaching of the monocline. Because the offset along the main normal faults is minimal (~20 m), the Nopolo structure is a unique example of an extensional faulted monocline and monocline system where faulting ended soon after the monoclines were breached and offset.

Keywords: Extensional monocline; Upward propagation; Normal fault

1. Introduction

Monoclines have long been associated with folding above reverse faults, such as the classic examples on the Colorado Plateau (e.g. Davis, 1978; Krantz, 1989; Davis, 1999). The monoclinal shape is dependent on the faults being widely spaced so that the outer limbs can maintain the subhorizontal geometry of true monoclines. Often, these structures form as drape folds above basement-cored uplifts related to reverse faults (Reches, 1978; Friedman et al., 1980; Chester et al., 1988). More recently, contractional monoclines were directly linked to the process of fault propagation (Mitra, 1993; Davis, 1999; Tindall and Davis, 1999).

Until recently, monoclines associated with extensional normal faults (Fig. 1) received much less attention than contractional monoclines (e.g. Hancock and Barka, 1987; Walsh and Watterson, 1987; Withjack et al., 1990; Patton et al., 1998; Gawthorpe et al., 1997; Gross et al., 1997; Janecke et al., 1998; Gardner et al., 1999; Sharp et al., 2000). This may be because when extensional folds are breached by normal faults they are commonly called drag folds, with an asymmetric syncline in the hanging wall and an open, asymmetric anticline in the footwall. Many of these drag folds are more likely fault-propagation folds (Mitra, 1993; Schlische, 1995) or forced folds (Withjack et al., 1990), but the process of fold development above a propagating normal fault is similar.

Experiments show that extensional monoclines are expected in layered rocks above the tip line of propagating normal faults (Fig. 1; Withjack et al., 1990; Couples et al., 1994; Couples and Lewis, 1998; Patton et al., 1998; Hardy and McClay, 1999; Withjack and Callaway, 2000). However, moderate to large normal fault systems that ceased being active during the initial stages of development are less common in nature. In these cases, the formation of the monoclines and the initial stages of faulting can be examined in detail.

In this paper, we describe the style and kinematics of the Nopolo structure near Loreto on the Baja California peninsula (Fig. 2). The Nopolo structure reflects the local 3D deformation associated with the upward and lateral

* Corresponding author. Present address: Montgomery Watson, 4525 South Wasatch Blvd., Salt Lake City, UT 84124, USA. Tel.: Harza, +1-928-523-6464.

E-mail address: paul.umhoefer@nau.edu (P.J. Umhoefer).

0191-8141/02/$ - see front matter
PII: S0191-8141(01)00120-1

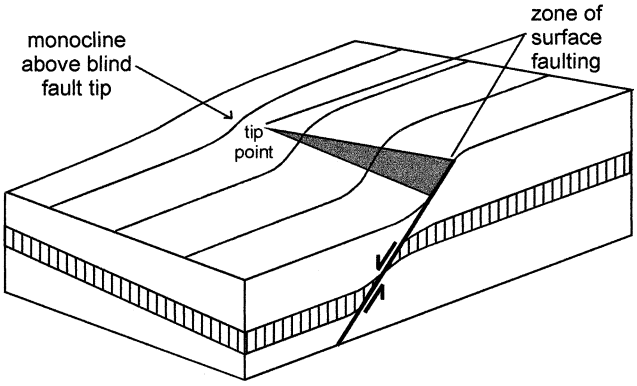

Fig. 1. Block diagram depicting along-strike variations in structural style of a propagating normal fault (after Gawthorpe et al., 1997)

termination of a relatively simple fault system that developed in a 2D regional strain field. We infer the 3D evolution of the structure using simple numerical modeling and by examining the current along-strike geometric variations that are likely a proxy for the temporal development of the structure. We compare the kinematics of the Nopolo structure to similar structures in the Gulf of Suez and in experimental studies. The Nopolo structure stopped at an early stage of development and therefore provides a rare snapshot of an extensional monocline that has been slightly modified by surface faulting. Other structures with greater structural relief (e.g. structures in the Gulf of Suez) presumably underwent similar deformation and so differences between these and the Nopolo structure may be attributed to protracted deformation. Extensional monoclines with limited fault offset also provide a key to the geometry of the hanging wall of large-displacement normal faults where the early structures are deeply buried. Our study suggests that folds along normal faults previously called drag folds are likely offset remnants of monoclines formed early in the evolution of normal faults.

2. Geologic setting

The Nopolo structure is part of the border fault system of the Loreto rift segment, located along the Gulf of California on the Baja California peninsula (Fig. 2a). The Loreto segment initially formed in the proto-gulf stage of the North American–Pacific plate boundary (Umhoefer et al., 1997, 2001b) from 12 to 6 Ma (Karig and Jensky, 1972; Hausback, 1984; Stock and Hodges, 1989; Stock and Lee, 1994). The proto-gulf stage was characterized by major transform faults west of the future Baja California peninsula along the newly formed Pacific–North American plate boundary at the same time that ENE–WSW-directed extensional structures developed within a former volcanic arc (Hausback, 1984; Stock and Hodges, 1989). Activity on normal faults across the inactive volcanic arc initially rifted the Baja California peninsula from mainland Mexico and lowered the landscape to form the proto-Gulf of California. After ~6 Ma, the present system of transform faults and short spreading ridges developed in the Gulf of California as the plate boundary largely jumped into the gulf (Lonsdale, 1989; DeMets, 1995).

The Loreto rift segment is one of many that formed along the Gulf of California (Axen, 1995). It is 85 km long and composed of four aligned structures (~335° strike) that are east-facing monoclines or normal faults (Fig. 2b; Umhoefer et al., 1997, 2001b). Strata east of the rift-bounding normal faults are tilted variably to the east and west in different parts of the Loreto rift segment. These variations in bedding attitude, and in relatively modest offsets on some of the rift-bounding structures, make it possible that larger east- or west-dipping faults lay offshore. Secondary faults in the region suggest that the Loreto segment and its four bounding structures formed in the late Miocene in a relatively simple 2D strain field with extension directed ~245– ~ 065°. The central part of the rift segment was overprinted in the Pliocene by the Loreto fault with a few kilometers of dextral-normal offset that formed the transtensional Loreto basin (Dorsey and Umhoefer, 2000). Active faulting on the Nopolo structure largely ceased at the end of the Miocene as faulting was concentrated on the adjacent Loreto fault (Fig. 2b). By the end of the Pliocene, most of the active faulting moved offshore, but the southern and northern parts of the fault system remained active in the Quaternary with low slip rates (Mayer and Vincent, 1999).

The Nopolo structure lies in the foothills of the Sierra de la Giganta, a steep, east-facing range that locally exceeds 1600 m in elevation (McLean, 1988; Zanchi, 1994). The crest of the Sierra de la Giganta is the drainage divide for the Baja California peninsula and is also referred to as the Main Gulf Escarpment, the topographic escarpment of the Gulf of California rift. West of the Nopolo structure, the Main Gulf Escarpment is lower (~500–1100 m elevation) than the rest of the Loreto segment (~800–1600 m elevation), probably because the Nopolo structure is no longer active. The region immediately east of the Sierra de la Giganta consists of flat-lying to ~5° east-dipping volcaniclastic rocks of the Miocene Comondú Group (Figs. 2b and 3b). The Comondú Group was formed in the volcanic arc and forearc basin that lay along northwestern Mexico before the Gulf of California formed (Hausback, 1984). In the area of the Nopolo structure, the middle and upper parts of the Comondú Group are exposed in the hanging wall as massive volcanic breccia and andesite lavas of the proximal and core facies of the arc (Fig. 3b; Hausback, 1984; McLean, 1988; Zanchi, 1994; Umhoefer et al., 2001a). The central and footwall parts of the Nopolo structure are underlain by the stratified clastic rocks of the lower unit of the Comondú Group (Fig. 3b; Umhoefer et al., 2001a). The lower clastic unit is composed mainly of interbedded sandstone and conglomerate in mixed proportions, tabular-bedded sandstone, and cross-bedded sandstone that

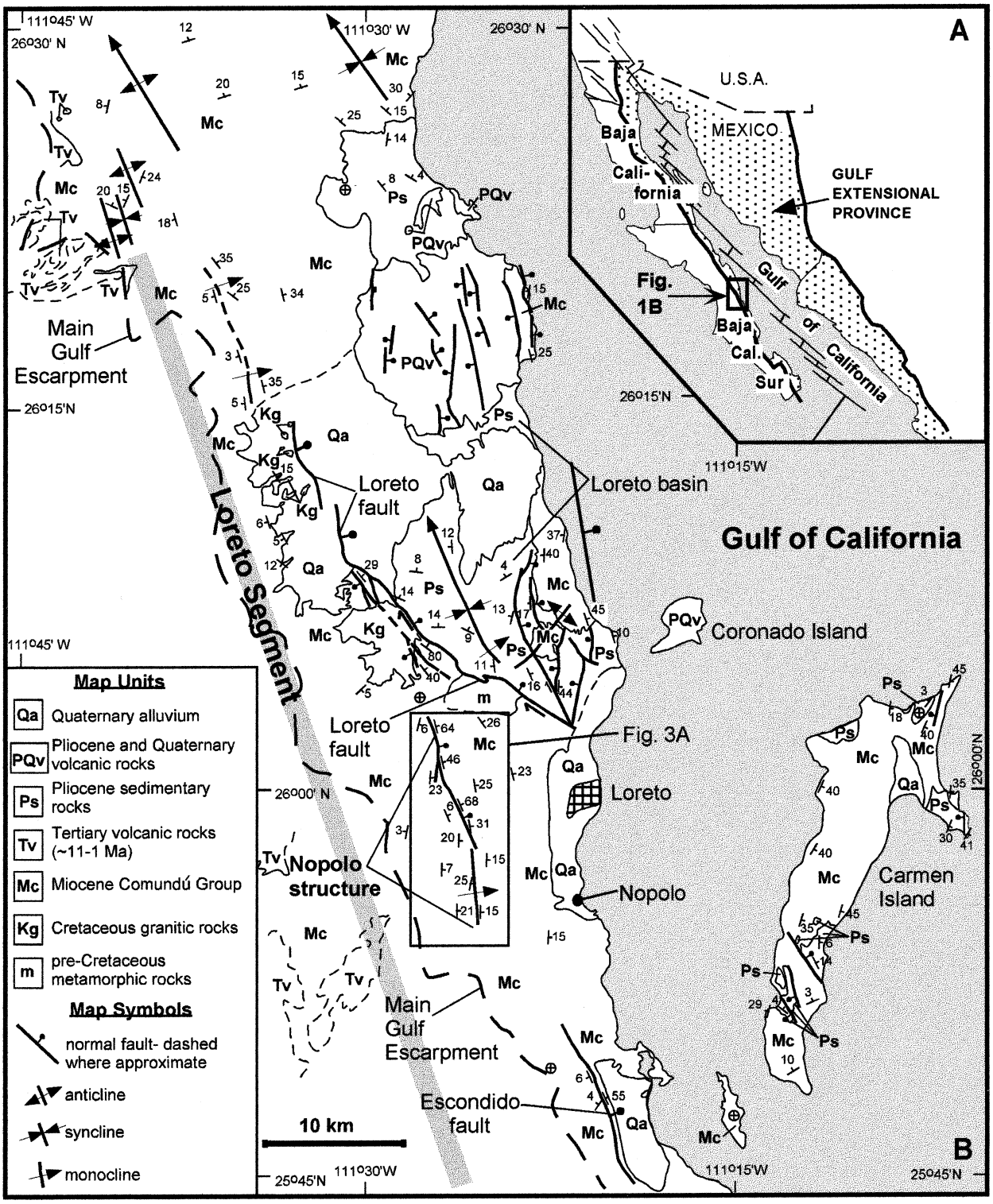

Fig. 2. (a) General tectonic map of the Gulf of California. (b) General geologic map of the Loreto rift segment (after Umhoefer et al., 2001b)

formed in a fluvial system with possibly local eolian deposits. Minor felsic tuffs and mafic lavas are important marker beds. The transition between the underlying lower clastic unit and the middle breccia unit is abrupt over a few meters and is also a key marker. The Comondú Group locally overlies Tertiary sandstone and Cretaceous granite at the northern end of the Nopolo structure.

In the region east of the Sierra de la Giganta, bedding gradually becomes steeper (up to 25°) eastward where it is cut by the main east-dipping normal faults of the Nopolo

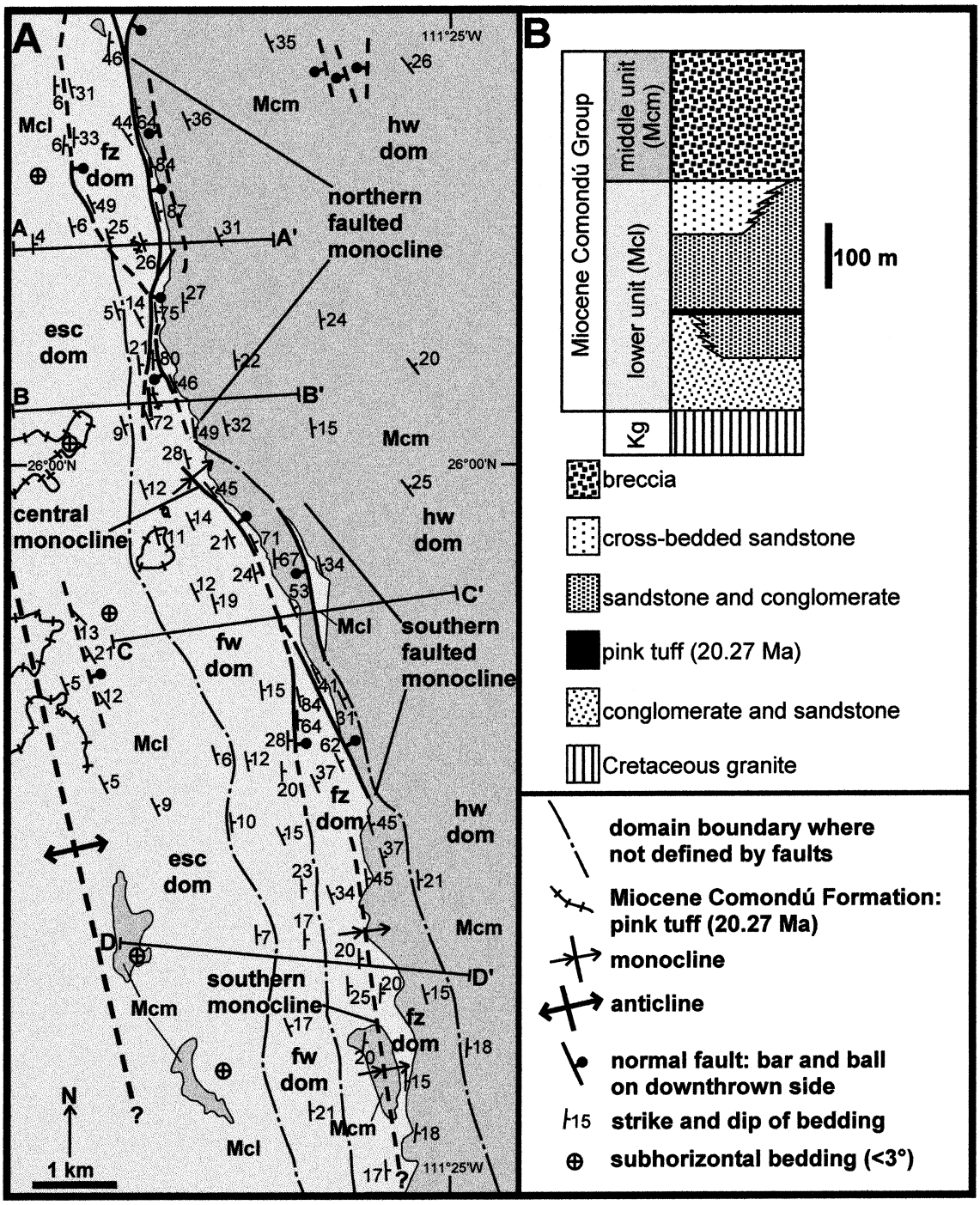

Fig. 3. (a) Simplified geologic map of the Nopolo structure showing key markers, major structures, and orientation of bedding. Structural domains are also shown: escarpment domain (esc dom), footwall domain (fw dom), fault zone domain (fz dom), and hanging wall domain (hw dom). Cross-sections A–A′ through D–D′ are shown in Fig. 4. (b) Generalized stratigraphic column showing lithologies of the lower and middle parts of the Comondú Group (after Umhoefer et al., 2001a).

structure. The structure consists of two normal-faulted monoclines with unbreached monoclines between and south of them (Figs. 3a and 4). Hanging wall strata within ~300 m of the Nopolo structure are steeply east-dipping to subvertical and are bounded by secondary antithetic normal faults and the main normal faults. East of these structures, the upper portion of the Comondú Group dips moderately to the east and extends to the coastal plain (Fig. 2b). Thus, the hanging wall of the Nopolo structure has been modified by continued normal faulting.

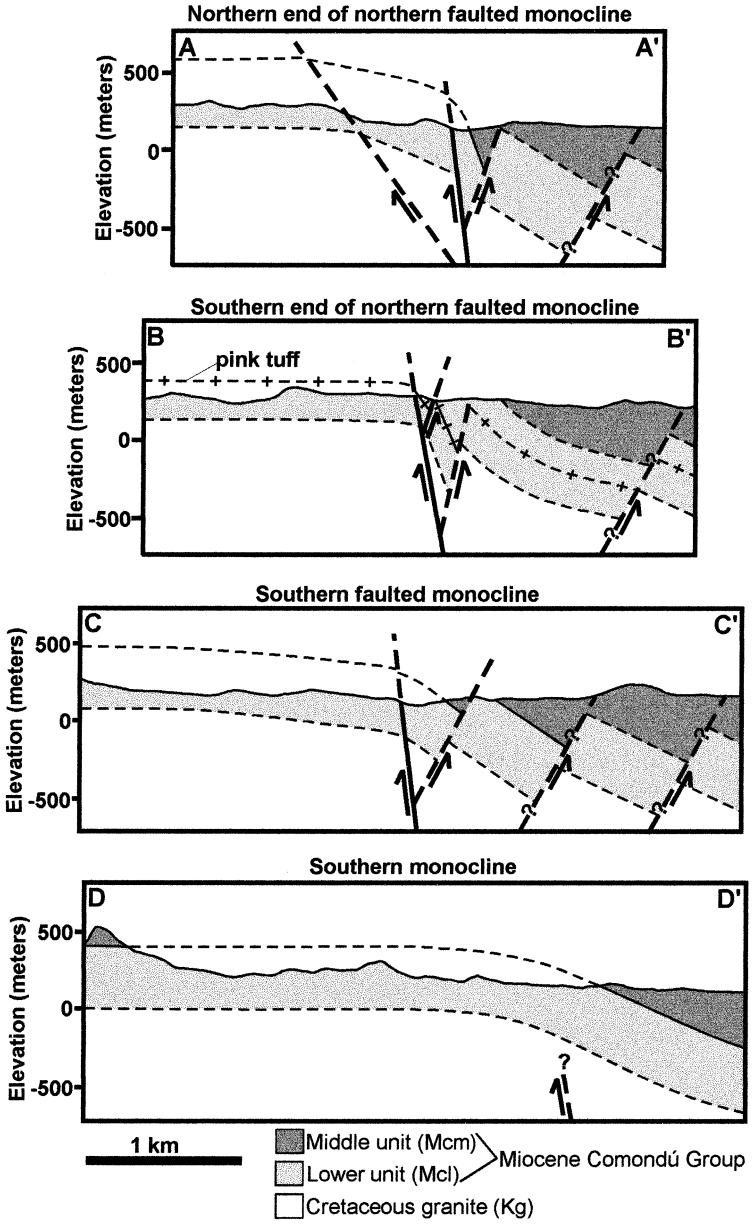

Fig. 4. Cross-sections A–A′ through D–D′ (see Fig. 3 for locations) depicting along-strike changes in structural geometry of the Nopolo structure.

3. Description and kinematics of the Nopolo structure

3.1. Methods

We describe the Nopolo structure from the footwall to the hanging wall and summarize the kinematics. The area of Fig. 3 was mapped at 1:20,000 scale with local 1:10,000 scale mapping. The kinematics of the Nopolo structure can be gleaned from abundant secondary (centimeter- to millimeter-scale) faults located near the structure. The validity of using these faults as regional kinematic indicators hinges on the assumption that faulting is scale-invariant, such that the kinematics observed on secondary faults mimics the larger structures. Sense of slip on each secondary fault was established by determining the down-stepping direction of slickenfibers (Petit, 1987). The kinematic analysis used the methods outlined in Marrett and Allmendinger (1990) and the program Faultkin 3.8a (Allmendinger et al., 1989) was used to analyze domains of faults and to present them in graphical form.

3.2. Structural domains

The region surrounding the Nopolo structure was divided into four major structural domains (Fig. 3a) based on bedding orientations, major fault locations, and structural style (i.e. proximity to fault and fracture zones, areas of folding). The main structural features associated with each domain are discussed below.

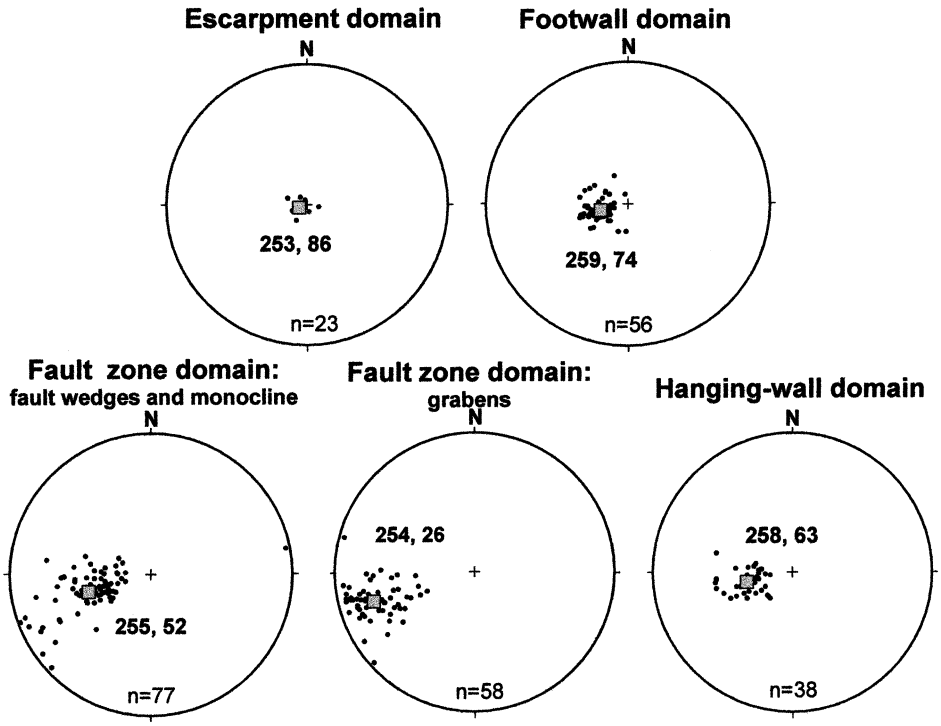

Fig. 5. Equal-area, lower hemisphere stereoplots showing poles to bedding for each structural domain. Orientation of mean vector is listed and shown by gray square.

3.2.1. Escarpment domain

The escarpment domain is located in the footwall, ~0.5–1 km west of the Nopolo structure (Fig. 3a). The only map-scale fault is an east-dipping normal fault with ~15 m of offset (Fig. 3a). Strata in the hanging wall of this fault dip gently to the west near the fault and become subhorizontal ~0.5 km to the east, defining a small, open rollover anticline. Another broad, open anticline is located near the western edge of the study area and trends NNW–SSE (Fig. 3a), subparallel to the overall strike of the Nopolo structure. Bedding is generally horizontal to ~10° east- and west-dipping (Fig. 5). Secondary faults show dominantly dip-slip motion and dip steeply to the east and west (Fig. 6). Faults strike NW–SE, but also strike N–S and NE–SW (Fig. 6). The kinematics of the faults within this domain yield an ENE–WSW extension direction (Fig. 6).

3.2.2. Footwall domain

The footwall domain consists of the immediate footwall region of the Nopolo structure and is noticeably more fractured and faulted than the escarpment domain. Bedding strikes NNW and dips gently to the east (Fig. 5). Bedding steepens from ~12° to ~25° as one approaches the main east-dipping normal faults of the Nopolo structure. Faults are typically small with offsets ranging from ~1 cm to ~5 m, exhibiting variability in both orientation and slip. Most faults are steeply to moderately west-dipping (Fig. 6). NW–SE striking faults dominate, with fewer N–S and NE–SW striking faults. The extension direction for the footwall domain is ENE–WSW (Fig. 6).

3.2.3. Fault zone domain

The fault zone domain is more intensely fractured (centimeter to millimeter spacing) and faulted (tens of meters to millimeter offset) than other domains and is located in the first ~300–500 m east of the main normal faults of the Nopolo structure or between normal fault splays. The Nopolo structure consists of four main structures that are located within this domain: a northern faulted monocline, a central monocline, a southern faulted monocline, and a southern monocline (Fig. 3a). The position and geometry of these structures suggest that they are controlled by two left-stepping, NW-striking normal faults. At its northern end, the northern faulted monocline has been overprinted by Pliocene faulting in the footwall of the Loreto fault (Fig. 2). To the south, the southern normal fault becomes blind and the southern monocline has formed above the inferred fault tip (Figs. 3a and 4). At the northern end of the southern faulted monocline, surface faulting dies out and is replaced by the steep (~45°) central monocline (Fig. 3a). Because the central monocline bends toward the northern faulted monocline, it may represent the link between the northern and southern normal faults.

The two main normal faults are well exposed only locally and are best defined by abrupt changes in the dip of bedding. In the footwall, strata dip very gently to gently to the east (5–25°; Fig. 3a). The first ~300 m of the hanging wall is an extremely fractured and faulted zone where strata are subvertical to steeply east-dipping (90–50°) and bounded by faults (Fig. 3a). The main east-dipping normal faults of the Nopolo structure typically have ~20–30 m of offset

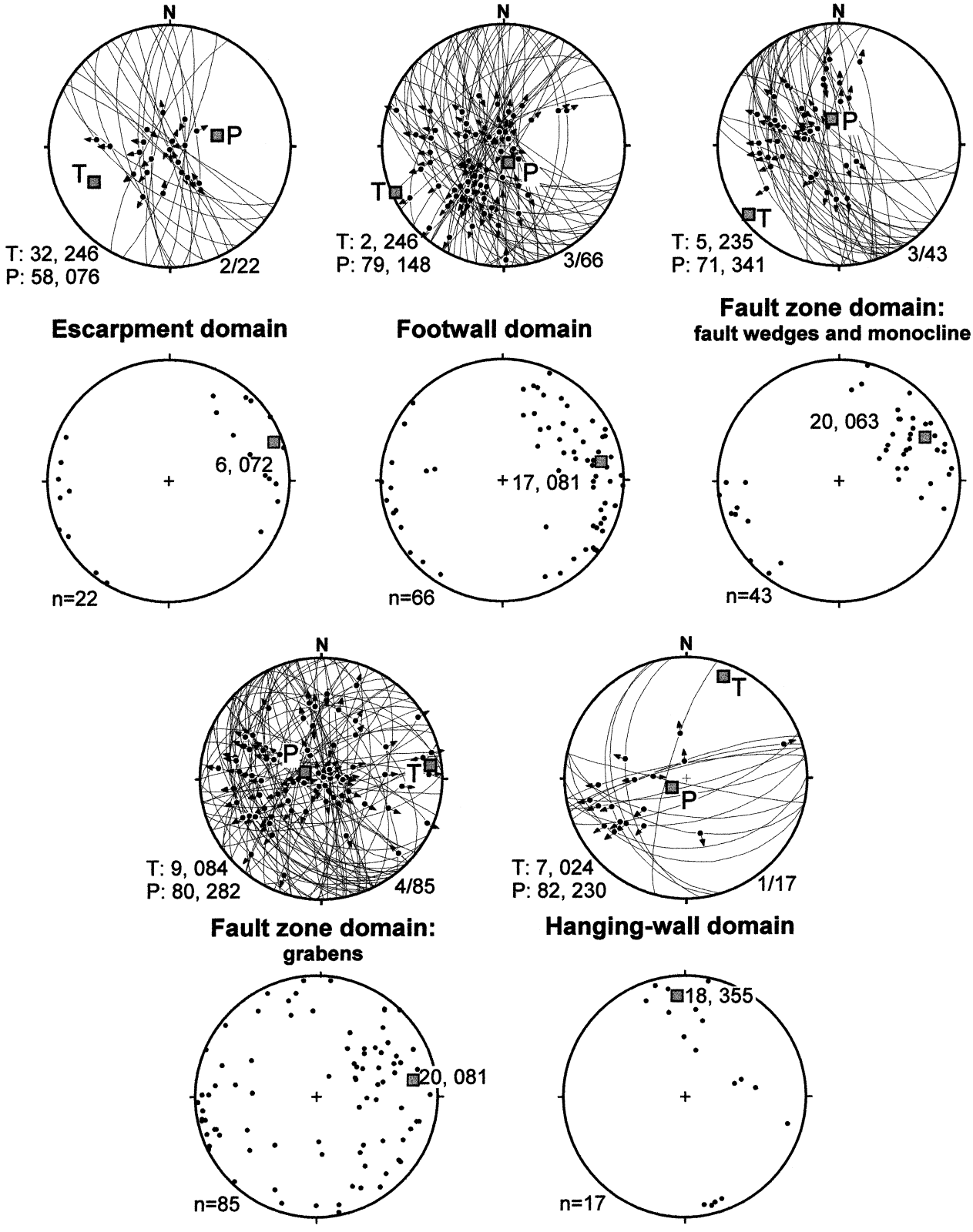

Fig. 6. Equal-area, lower hemisphere stereoplots of secondary faults for each structural domain (see Fig. 3). Top stereoplot for each domain is fault planes (arrows on faults represent slip direction of the hanging wall). Determined *P* and *T* axes for each domain shown by gray boxes. Ratio at lower right of top stereoplot is number of faults of total population that fall outside determined *P* and *T* regions of domain by $>10°$. Orientation of domainal *P* and *T* axes listed at lower left of each stereoplot. Bottom stereoplot is poles to faults and best fit mean vector (gray boxes) for each domain. Trend and plunge of each mean vector is given.

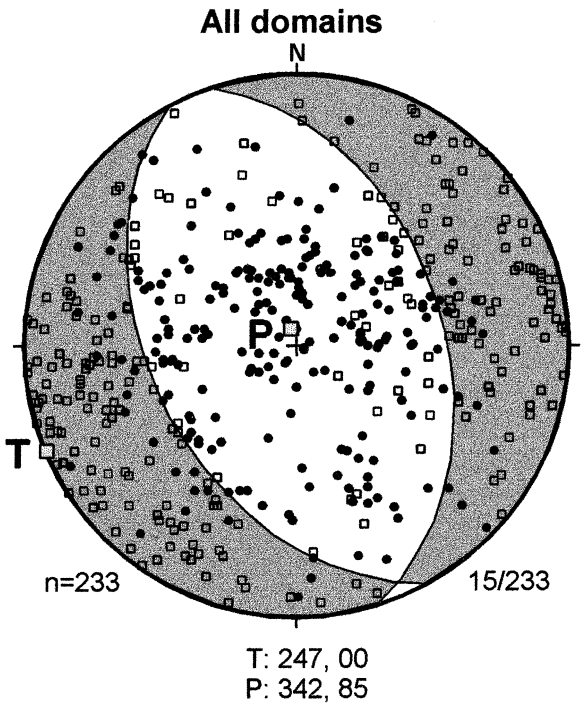

Fig. 7. Fault plane solution showing *P* and *T* axes for secondary faults from all domains. Black dots are *P* axes, open squares are *T* axes. Large gray squares are calculated *P* and *T* axes for all faults. Ratio at lower right is number of faults that fall outside combined *P* and *T* regions by >10°. Orientation of combined *P* and *T* axes listed at bottom.

(Fig. 4). Secondary splays have offsets ranging from a few millimeters to ~15 m.

The fault zone domain contains three subdomains; grabens, fault wedges, and the southern monocline. Grabens are centered on the northern and southern faulted monoclines and are bounded by the main east-dipping normal faults on the west and antithetic hanging wall normal faults on the east. Bedding strikes NNW, dipping steeply to the east (Fig. 5). Generally, faults are dip-slip, strike NW–SE to N–S and dip steeply to moderately to the west and east (Fig. 6). The extension direction for the graben subdomain is ~E–W (Fig. 6).

The fault wedge subdomain is bounded by the main east-dipping normal faults and synthetic normal faults. One fault wedge located at the northern end of the northern faulted monocline (Fig. 3a) contains strata that are moderately dipping with slight steepening to the west near the synthetic normal fault. Another fault wedge located at the southern end of the southern faulted monocline (Fig. 3a) contains east-dipping strata that steepen with proximity to the faults.

The southern monocline is located south of the southern faulted monocline and contains no map-scale faults. Small faults with up to ~1–2 m of offset are common, but fractures accommodate much of the dilation. These fractures are concentrated in discrete zones that are 10–50 m wide, are mostly subvertical, and are spaced every millimeter to centimeter.

The fault wedges and the southern monocline were combined into one subdomain due to similarities in bedding and fault orientations. Bedding strikes NNW and dips moderately to the east (Fig. 5). Secondary normal faults dominantly strike NW–SE and dip steeply to moderately to the west (Fig. 6). The extension direction for this subdomain is NE–SW (Fig. 6).

3.2.4. Hanging wall domain

The hanging wall domain is a zone of less pronounced faulting located east of the fault zone domain. This region contains primarily massive and variably weathered volcanic breccia of the middle part of the Comondú Group. This region probably contains several moderate to large west-dipping faults based on the eastward persistence of the middle breccia unit and consistent east-dipping bedding (15–35°). However, the massive nature of the breccia makes faults and bedding difficult to identify. A lava marker in the middle breccia unit in the northeast part of the map area revealed west-dipping normal faults spaced every few hundred meters (Fig. 3a). Fractures are also dominantly west-dipping. The inferred faults are not shown in Fig. 3a, but are postulated in Fig. 4.

Bedding in the hanging wall domain strikes NNW and dips gently to moderately to the east (Fig. 5). Faults mainly strike ENE–WSW and dip steeply to moderately to the NW and SE (Fig. 6). The inferred extension direction for the hanging wall domain is ~NE–SW (Fig. 6).

3.3. Offset across Nopolo structure

The formation of the monoclines produced the majority of structural relief and was followed by minimal displacement surface faulting. The amount of down-to-the-east structural relief produced by the monocline was calculated by using the base of the middle breccia unit or a pink tuff in the lower clastic unit as an offset marker. Because strata are tilted ~25° east in the hanging wall, the eastern flat of the monocline is not exposed, so the amount of structural relief given for each cross-section is considered a minimum value.

In cross-section A–A′ (Fig. 4), the amount of structural relief is ~370 m. The western and main normal faults show down-to-the-east offsets of ~10 and 20 m, respectively. These offsets are imperceptible at the scale shown in the cross-section in Fig. 4. In cross-section B–B′ (Fig. 4), ~300 m of structural relief is estimated. The main and antithetic normal faults have ~20 and ~90 m of down-to-the-east offset, respectively. In cross-section C–C′ (Fig. 4), ~330 m of structural relief is estimated. The main and antithetic normal faults have ~30 and ~190 m of down-to-the-east offset, respectively. The structural relief across cross-section D–D′ (Fig. 4) is ~330 m and contains no known surface faults.

3.4. Summary of domain analysis

A cumulative plot of all kinematic data yields a fault-plane solution showing nearly pure dip-slip motion with a

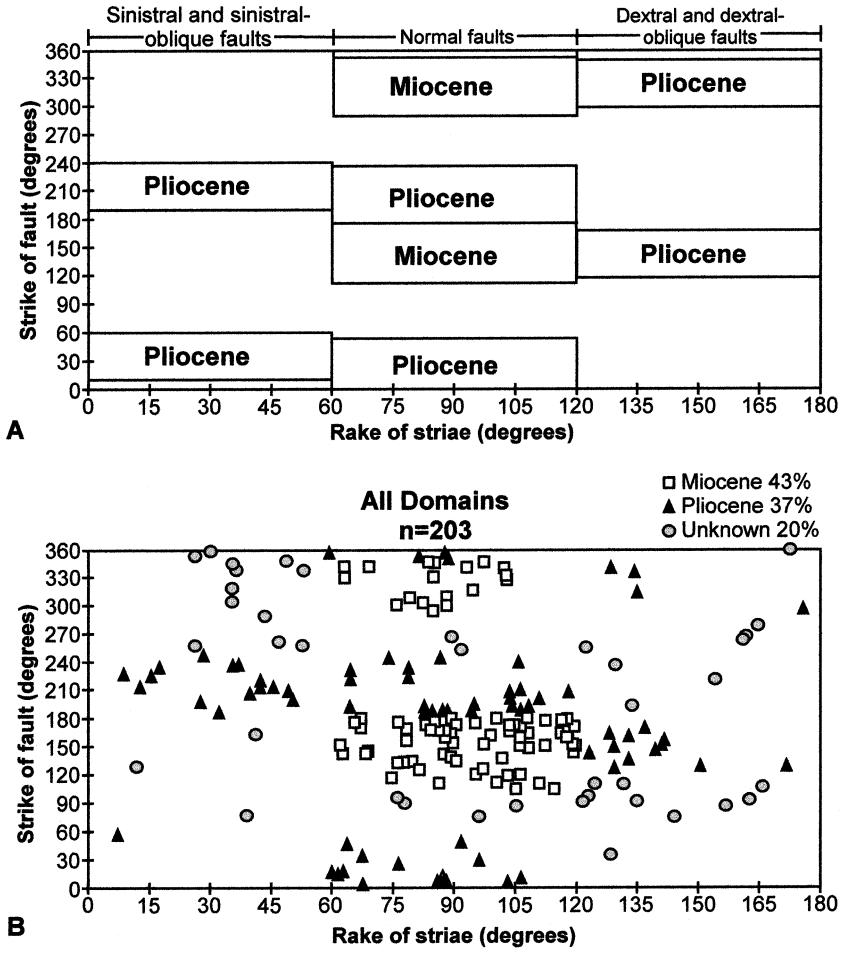

Fig. 8. (a) Strike and rake values that define idealized Pliocene- and Miocene-age faults (see text for discussion). (b) Graph of strike versus rake for secondary faults in all domains. Boxes are likely Miocene faults, triangles are likely Pliocene faults, circles are faults of unknown age. Percentages of each are given in upper right corner.

T-axis orientation of 0°, 247° and a *P*-axis orientation of 85°, 342° (Fig. 7). The domainal plots in Fig. 6 show that local variations in the extension direction exist. However, the fault plane solution in Fig. 7 is considered robust because even though 15% of the individual *P* or *T* axes lie strictly outside the determined *P* or *T* regions, only 6% of the *P* or *T* axes are located outside by more than 10°.

The extension direction presented here (247°) agrees closely with the extension direction (244°) suggested by Umhoefer et al. (2001b) during the late Miocene for the entire Loreto segment. Late Miocene faulting was part of the proto-gulf stage of development (12–6 Ma) where extension was accomplished along NW–SE-striking normal faults (Hausback, 1984; Stock and Hodges, 1989). The extension directions mentioned above are nearly perpendicular to the overall strike (335°) of the main structures in the Loreto segment, suggesting that these structures initiated in late Miocene time.

The results of the kinematic analysis show that secondary faults of the Nopolo structure are consistent with the late Miocene extension direction. The presence of oblique-slip and strike-slip secondary faults suggests oblique overprinting during the Pliocene.

4. Role of oblique overprinting

Based on the results of the kinematic analysis, Miocene rocks in the Nopolo structure were deformed during the orthogonal rifting phase (12–6 Ma). A direct record of oblique rifting (6–0 Ma) is unavailable because the structure contains no Pliocene rocks. Additionally, there are no map-scale faults consistent with the Pliocene extension direction (~280°; Zanchi, 1994; Umhoefer and Stone, 1996; Dorsey and Umhoefer, 2000).

We explored the possibility of overprinting by the Pliocene strain field using the ~280° extension direction. We differentiated Miocene faults from Pliocene faults by comparing the kinematics of secondary faults that coincided with either the Miocene strain field (extension direction of

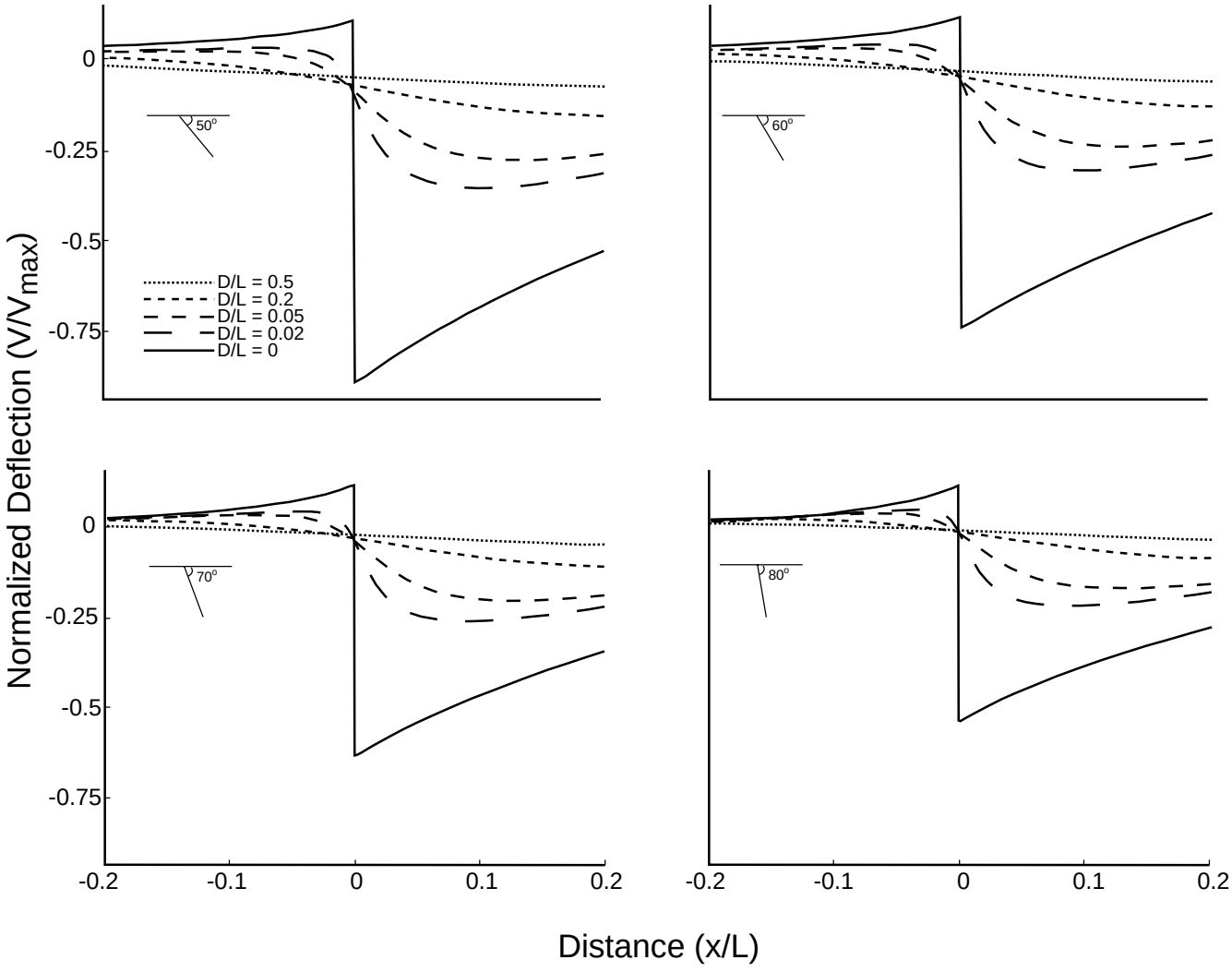

Fig. 9. Deflection resulting from a uniform stress drop along planar normal faults dipping 50, 60, 70, and 80° whose upper tips are located 0.5, 0.2, 0.05, 0.02, and 0 times the fault length below the surface. Where the blind fault tip is located farther from the surface, the amplitude of the monocline decreases. There are subtle differences in the deflection due to fault dip; however, these effects are minor in comparison to the depth of the fault tip (e.g. Withjack et al., 1990).

~245°; Henry, 1989; Stock and Hodges, 1989; Umhoefer et al., 2001b; this study) or the Pliocene strain field (extension direction of ~280°). Fig. 8a shows the age classification (Miocene and Pliocene) assigned to a given range of fault strike and rake. Overlap between Miocene and Pliocene normal fault orientations was reconciled by using the midpoints between the two extension directions (173° and 353°). Based on the scatter of data points shown in Fig. 8b, normal faults were given a 63° range, whereas oblique- and strike-slip faults were given a 50° range.

Based on the total number of faults in all domains, Miocene and Pliocene faults account for 43 and 37%, respectively (Fig. 8b). This suggests that a significant portion of secondary faults in the Nopolo structure record Pliocene oblique deformation. Based on this analysis, small Pliocene faults are nearly as numerous as small Miocene faults (Fig. 8b) and are mainly concentrated in the northern part of the study area, closer to the Pliocene Loreto fault (Fig. 2b). Slickenlines and slickenfibers record the most recent episode of faulting and possibly obliterate earlier faulting events. Therefore, it is likely that small Pliocene faults are more prevalent in this analysis because they reactivated Miocene faults and destroyed earlier kinematic indicators. However, because there are no map-scale faults whose orientation is consistent with the Pliocene strain field, we conclude that the overall effects of overprinting were minor and did not substantially change the Nopolo structure's geometry. It is worth noting, however, that the left-stepping alignment of the rift-defining structures (Fig. 2b) and the Nopolo structure (Fig. 3a) is consistent with model results for dextral-oblique shear and may indicate that these rift-defining structures were approximately linear prior to ~6 Ma and were subsequently offset during 0–6 Ma (Tron and Brun, 1991; Smith and Durney, 1992).

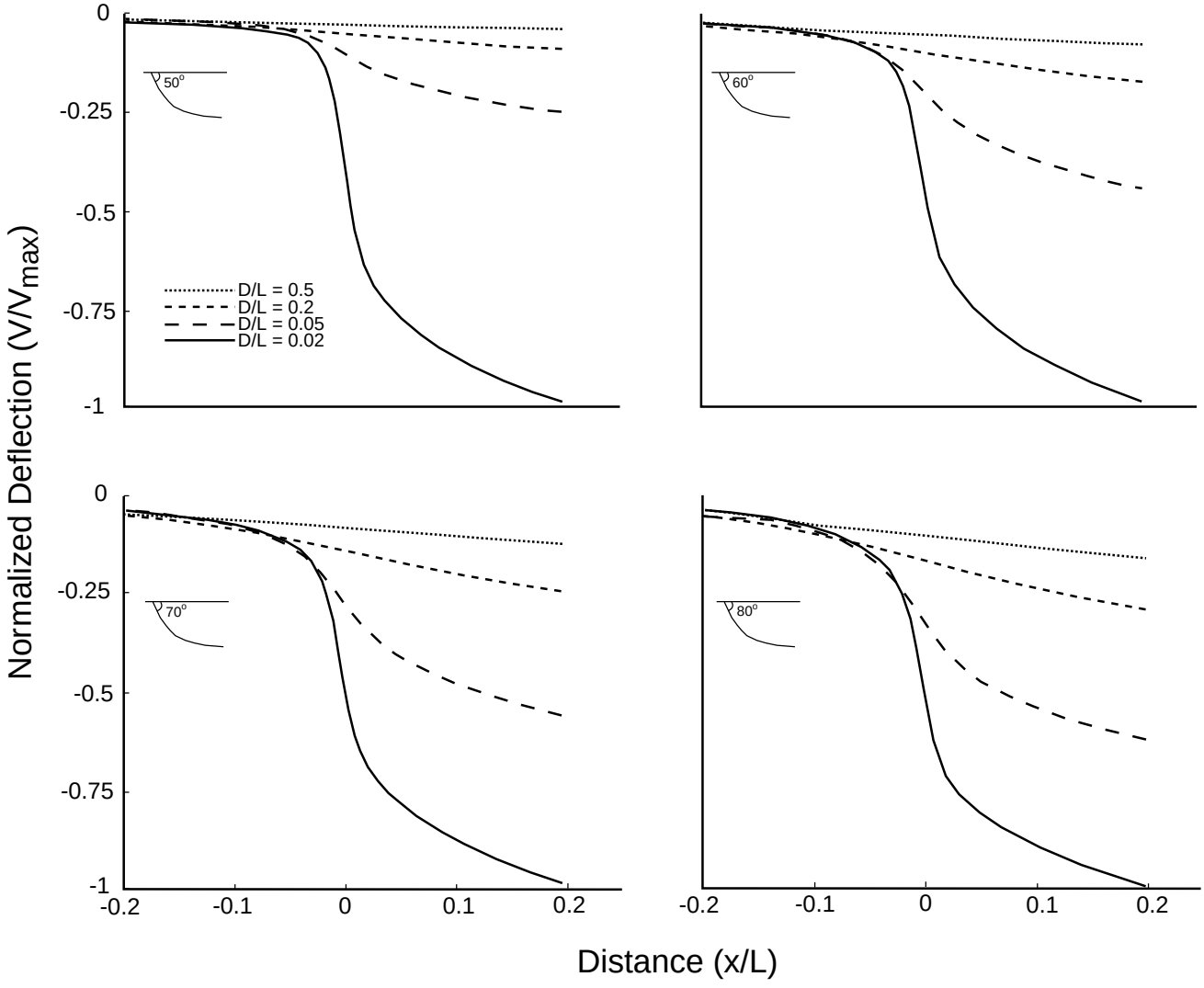

Fig. 10. Deflection resulting from a uniform remote stress drop resolved onto listric normal faults whose upper tips are located 0.5, 0.2, 0.05, and 0.02 times the flattening depth of the fault below the surface. The dip at the upper tip of the fault in each panel is 50, 60, 70, and 80° and decreases monotonically with depth. As with planar normal faults, the deflection becomes more subtle as the fault tip is located farther below the surface. Importantly, surface deflections and tilts persist for large distances (relative to the fault's flattening depth), in contrast to the surface deflections produced by planar faults.

5. Modeling

5.1. Forward models of deformation around normal faults

Our detailed field studies gave us a limited 3D view of the Nopolo structure by using along-strike variations as proxies for the temporal evolution of the breached monoclines. Here we discuss numerical modeling that we employed after the field study in order to better understand the geometry of the structure in 3D. Numerical models of crustal deformation allow us to link observed displacement patterns to the stresses that caused those displacements. In particular, by measuring bedding-plane tilts (dip) across the Nopolo structure, we inferred the geometry of the fault that is required to create the observed tilts.

In our modeling study, we used boundary element models to compute the surface deflections and bedding tilts near a blind normal fault. First, we created a 2D boundary element model (BEM) to understand how normal fault-driven monoclines (whose along-strike length is long relative to its wavelength) deflect and tilt bedding near the surface. Then, we used a 3D BEM to investigate how bedding tilts change with along-strike variations in the structure's geometry. In our 2D models, we used bedding-plane tilts measured perpendicular to the strike of the Nopolo monocline to gain a first-order estimate of the fault geometry at depth. Then, we used a 3D BEM to qualitatively understand the along-strike variations in deflection around the Nopolo structure and how monoclinal breaching may change the deflection field.

5.2. 2D (profile) modeling of surface deflection and tilt around normal faults

Our 2D BEM idealizes the upper crust of the Earth as a

continuous, linear elastic half-space subject to plane-strain conditions in the out-of-plane dimension (e.g. Jaeger and Cook, 1976; Segall and Pollard, 1980). We assume that the stresses and strains are continuous at all points except the fault, where we introduce a frictionless displacement discontinuity in the medium. Allowing the two sides of the discontinuity to slip past one another simulates slip along a fault. In our static models, there is no time-dependent loading or relaxation of the material. Slip along the faults is driven by a constant stress drop along their down-dip length. We also assume that as the fault becomes small relative to the length of the model, perturbations in the stress and strain fields induced by slip along the fault will become spatially restricted and insignificant as slip decreases. Therefore, the stresses and strains resulting from fault movement become zero at an infinite distance from the fault.

Frictionless faults that undergo a constant stress drop must have non-uniform displacements along their surface (Crouch and Starfield, 1983) because slip along one section of a fault may transfer stress to other parts of the fault, and thus, enhance the slip along the loaded section. In order to create a constant stress drop across the fault, we discritized the fault plane into a series of 50 connected elements and let each slip a sufficient amount required to create a uniform stress drop along the down-dip fault length (e.g. Crouch and Starfield, 1983).

Linear–elastic, fracture-mechanics models may be used to either understand the deformation field as different physical or geometric properties of the system are changed (forward model), or to constrain physical or geometric properties of the system based on field observations of the deformation (inverse model). The following section explores the effect of different fault geometries on surface displacements and deflection, whereas subsequent sections constrain fault geometries using derivatives of the surface deflection (bedding tilts).

5.2.1. Forward models of deflection around normal faults

We calculated the surface deflection due to a stress drop along both planar and listric normal faults that dipped 50, 60, 70, and 80°, and whose upper tip depths were 0.5, 0.2, 0.05, 0.02, and 0 times the length of the fault (Figs. 9 and 10). The surface deflection profiles show a cross-section through each modeled fault, which undergoes a constant uniform stress drop. We assume a shear modulus (G) of 30 GPa, and a Poisson's ratio (ν) of 0.25 (Clark, 1966). Neglecting lithostatic stresses from the model: (1) creates a simplified model that is not scale-dependent; (2) allows us to observe the first-order deformational patterns at all spatial scales; and (3) has no effect on fault orientation since the fault is frictionless. In our scale-independent model, the deflection gradient scales linearly with the fault length and the horizontal distance perpendicular to the fault tip can be normalized to the length of the fault (D/L). For example, 1 m of slip along a fault that dips 45° and extends to 1 km depth produces the same surface displacement at a distance of 2 km from the fault tip as a fault that extends to a depth of 10 km at a distance of 20 km away from the fault tip. Our models are scaled to an arbitrary length, L. For the planar fault models, L was chosen as the fault length, whereas in the listric fault models, L is the depth at which the fault plane becomes horizontal. In each model, the depth to the upper fault tip, D, is normalized to this length scale. Finally, the deflection, V, is normalized to the value of maximum offset (V_{max}) when the fault reaches the surface for all models.

For planar faults, monoclines are formed when the tip of the fault does not reach the surface ($D/L = 0.5$, 0.2, 0.05, and 0.02). The amplitude of the monocline is inversely proportional to the depth to the tip of the fault, whereas the wavelength is directly proportional to the down-dip fault length (Fig. 9). When the fault reaches the surface, the offset is localized along a single failure plane. In our models, increasing dip lessens the maximum offset along the fault, as faults oriented more parallel to the free surface slip more for a given stress drop.

When faults are listric, the surface deflection does not rapidly decay with horizontal distance from the fault tip. In the hanging wall, deflections and bedding-plane tilts are maintained for large distances relative to the sole-out depth (Fig. 10). Increasing fault dip accentuates the hanging wall surface deflection. In contrast, deflections within the footwall remain modest and decay rapidly away from the fault.

Our models suggest that the down-dip fault geometry (planar vs. listric) and the location of the fault tip relative to the size of the fault exerts a primary control on the surface deflections (e.g. Cooke, 1996). The fault dip changes the deformation field, but this effect is subtle in contrast to the effects of geometry and fault-tip depth. The models indicate that the amplitude of the monocline always increases as the fault tip approaches the surface of the earth, and that regional (>15 km) deflections and bedding-plane tilts require listric fault geometries. These qualitative observations can be used to estimate the down-dip fault geometry, extent, and tip-line location of faults.

In areas where the deflection or tilt can be measured, the fault geometry, depth to the upper fault tip, and the fault dip can be estimated. The relative deflection and tilt are relatively insensitive to fault dip and, therefore, surface measurements of fault orientations provide more constrained measures of the fault orientation. However, the deflection and tilt are sensitive to depth to the upper tip of the fault and down-dip geometry of the fault. Therefore, if variations in monocline geometry can be measured along strike, a 3D picture of the fault geometry may be inferred.

5.2.2. Inferring down-dip fault geometry of the Nopolo structure from bedding-plane orientations (inverse models)

In addition to using the 2D BEM to understand how surface deflections and tilts may change as fault-tip depth,

Table 1
Inversion results for the two structural models (planar vs. listric normal fault) and two weighting schemes investigated. Values in italics indicate that the inversion reached one of its imposed constraints. The model that best fits the data is a listric normal fault that flattens at ~5 km depth (Inversion 4). See text for discussion

	Inversion 1 Planar fault Weighting 1	Inversion 2 Planar fault Weighting 2	Inversion 3 Listric fault Weighting 1	Inversion 4 Listric fault Weighting 2
A–A′ fault length (m)	13766	12137	N/A	N/A
A–A′ upper tip depth (m)	*3000*	*5000*	700.1	1018.8
B–B′ fault length (m)	*15000*	12598	N/A	N/A
B–B′ upper tip depth (m)	*3000*	*5000*	668.7	958.8
C–C′ fault length (m)	13377	11943	N/A	N/A
C–C′ upper tip depth (m)	*3000*	*5000*	676.9	965.3
D–D′ fault length (m)	12001	12312	N/A	N/A
D–D′ upper tip depth (m)	*3000*	*5000*	927.4	1172
Fault dip (°)	80	90	90	90
Flattening depth (m)	N/A	N/A	5000	5173.5
RMS	0.06226	0.04828	0.03389	0.02184

dip, down-dip geometry, length, and horizontal position change, we used the model to infer these geometric fault properties from the tilt of bedding planes. Here, the model is used in an inverse sense to infer the approximate down-dip geometry of the fault that tilted bedding within the Nopolo structure.

Field observations suggest a two-stage development of the structure. First, monoclinal flexing of sedimentary strata likely occurred when the normal fault was blind. Following flexure, the fault propagated towards the surface and breached the monocline. Because the amount of offset of the breached monocline is small (tens of meters) relative to the amplitude of the fold (hundreds of meters), we infer that most bedding-plane tilts are primarily the result of monoclinal flexure when the fault was blind. In general, bedding measurements around the Nopolo structure steepen toward the center of the monocline, and show a marked asymmetry towards the east.

Both planar and listric fault geometries were considered for determining the model fault geometry that best fit the bedding data. In addition, bedding tilts were weighted according to the likelihood of post-breaching offsets affecting bedding tilt. Therefore, measurements within the fault zone that were presumably affected by post-monoclinal faulting were weighted less than points outside the fault zone. The best-fitting fault geometry was determined for each of four different cross-sections (Fig. 4). We employed a least-squares numerical inversion to find the global minimum of the root-mean square error (RMS) for all combinations of the fault geometry parameters (model parameters) for all four cross-sections. Our analysis implicitly assumes: (1) the earth behaves as a linear elastic half-space with continuous stresses and strains at all points but the fault plane; (2) movement along the fault is driven by a complete stress drop that is determined by resolving a unit remote tension in the direction parallel to the profile onto the fault surface; (3) the tilts and deflections scale linearly with the total amount of stress drop along the fault surface; (4) no opening tractions act on the fault surface; (5) the fault surface is frictionless; and (6) the layers being warped are near the earth's surface. Our inversion used elastic values typical of the upper crust ($\nu = 0.25$, $G = 30$ GPa).

Because the tangent of the tilt angles and deflections in our model scale linearly with the total stress drop (and hence fault slip), the spatial distribution of tilts can be normalized to directly compare tilts measured around the monocline to those produced by the normalized tilts in the model. For example, doubling the stress drop (and hence, fault slip) doubles the tangent of the tilts in our model. We normalized all modeled tilts to the tilt at a constant location, so that the resulting normalized tilt distribution depends only on the fault geometry, length, tip depth and the tilt value at the position chosen to normalize the tilts. By comparing the normalized modeled tilts to measured tilts that have been normalized to the same location as the model values, the normalized observed and modeled tilts were directly compared.

Two weighting schemes were devised for both planar and listric faults to emphasize tilts that formed prior to monoclinal breaching. The bedding data were initially classified by their proximity to a fault zone with the following weighting scheme; 1 = point directly in fault zone, 2 = point may be affected by tilting within fault zone, 3 = point unaffected by fault zone. These classifications were weighted to two scales. In the first, each category received the weight of its code, whereas in the second, points directly in the fault zone, points that may be affected by tilting within the fault zone, and points unaffected by the fault zone were given weights of 1, 3, and 5, respectively. A weighted average of the dips was determined for each of the different schemes. For each scheme, the tilts were normalized by the weighted average of all tilts in each profile. The same process was applied to the modeled tilt, allowing a direct comparison of the bedding orientations with the modeled surface tilt. The RMS value between the measured and modeled tilts was calculated and minimized.

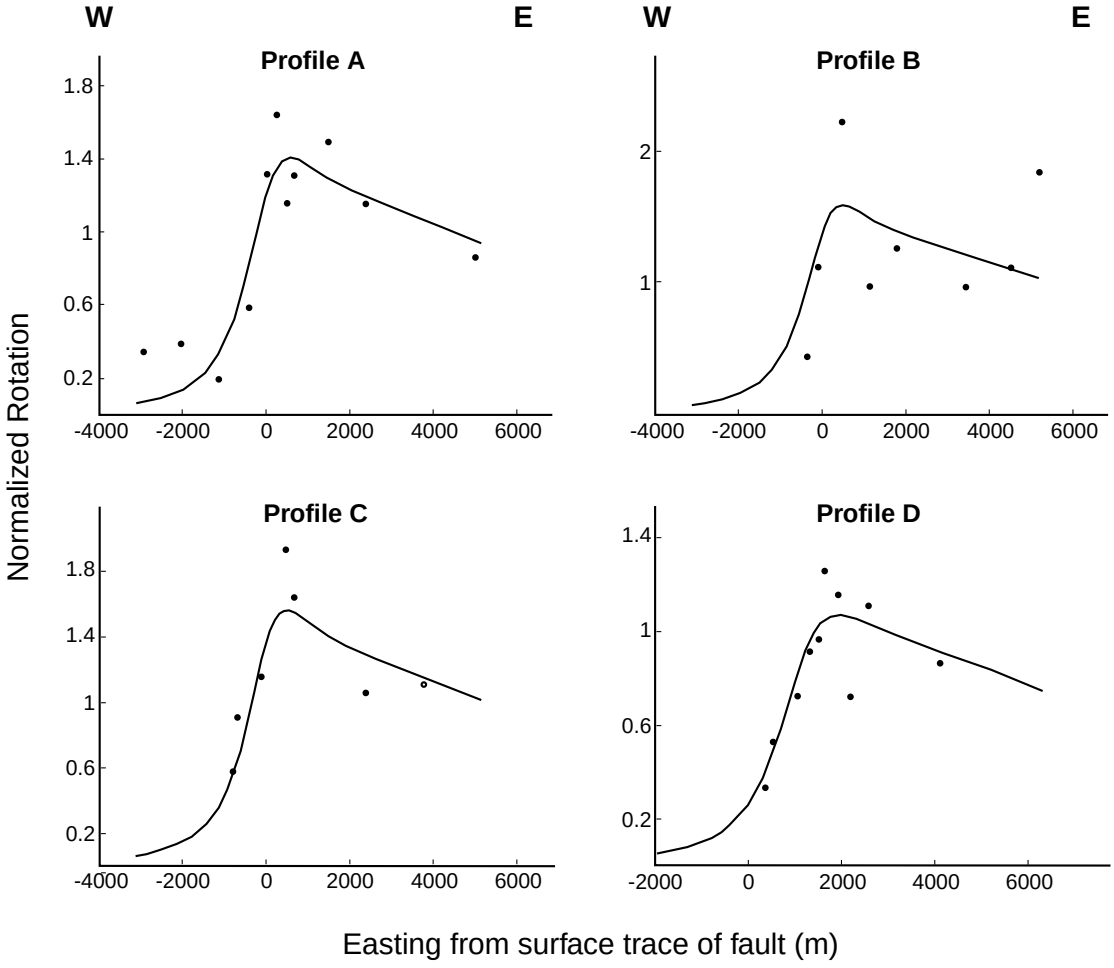

Fig. 11. Best-fit model fault geometry for the Nopolo structure. Each plot shows a cross-section through the structure (see Fig. 3 for cross-section locations). The points in each figure show the measured tilt normalized to the weighted average of all tilts as a function of distance from the surface trace of the monocline-breaching fault. The solid line shows the normalized tilts that are produced by the best-fit model fault geometry (Inversion 4; Table 1). In this inversion, the fault geometry is listric with a flattening depth of 5173 m below the surface. The model suggests that the listric normal fault was blind with the tip 1 km below the surface (1018.8, 958.8, 965.3, and 1172 m for profiles A–A′, B–B′, C–C′, and D–D′, respectively). In general, the fault's tip line is closest to the surface at the center of the structure and becomes deeper towards the ends of the structure.

Four inversions were performed that explored the effect of the two different weighting schemes applied to two different fault geometries (planar and listric). In all models, an 80 or 90° fault dip was used and the fault-tip location and down-dip fault length varied between profiles. In Inversion 1, the upper fault tip was constrained to a maximum depth of 3 km, whereas in Inversion 2, this depth extends to 5 km. In the listric fault models, the depth to the upper tip varied between profiles, but the depth at which the fault flattens was kept constant. The results of the inversions are shown in Table 1.

The bedding data were best fit by a listric normal fault whose upper tip was located 900–1200 m below the surface, and which flattened just below 5 km (Table 1, Inversion 4; Fig. 11). For each fault geometry, the fit improved when points near or in the fault zone were weighted less. A sensitivity analysis for each of the inversions revealed that the sole-out depth and upper fault dip locations were better defined than the fault dip. The cross-section data fit the model relatively well, with the exception of the B–B′ cross-section (Fig. 11). From these models, we presume that the majority of the bedding tilt in the region resulted from a blind listric normal fault that soled out between 4 and 6 km and whose tip was located 500–1500 m below the earth's surface.

The assumptions of mechanical quasi-static equilibrium of a linear elastic medium allows normalization of the length scale, deflection, and tilts in the model. These assumptions also neglect the presumably important time-dependent stress relaxation effects that result in irrecoverable strain in the material. While such rheologic responses may more appropriately model deformation in the upper crust, they also introduce a correspondingly larger number of free parameters into the problem, which may be difficult or impossible to constrain with available field data. In addition, introducing greater complexities into the models

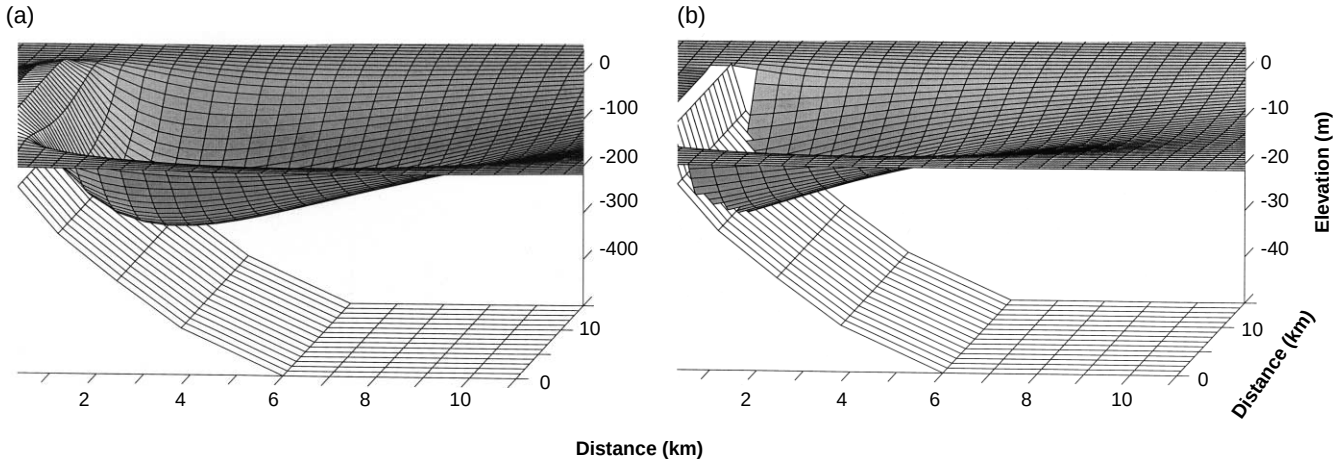

Fig. 12. 3D deflection around a listric normal fault. (a) The tip line of the fault is located 1 km below the earth's surface. A monocline develops above the fault and decreases in amplitude towards the ends of the fault. (b) As the fault breaches the monocline, bedding-plane rotation is not significant in the footwall of the normal fault and changes sense in the hanging wall near the fault, relative to the case where the fault has not reached the surface (a).

may prevent numerical inversions from reaching a global minimum in a realistic amount of time. Therefore, while our models are relatively simple, they highlight at least the first-order controls on deformation and provide bounded constraints on the fault geometries inferred from bedding tilts around normal faults.

5.3. 3D deformation around the Nopolo structure

By using the 2D geometry inferred for each cross-section along the Nopolo structure, we built a 3D boundary element model of the fault to qualitatively understand the 3D effects of the fault geometry on the surface deflection. In addition, we considered the two deflection fields that result from the stages when the fault is blind and when surface faulting begins to understand the change in the surface deflection that may have accompanied breaching of the monocline. We inferred the 3D displacement field that may have led to the formation of the Nopolo structure using a 3D polygonal boundary element model, Poly3D (Thomas, 1993). This model assumes that the upper crust of the Earth deforms as a homogeneous, linear elastic half-space and that the fault is frictionless. We used the best-fit modeled fault geometry from our plane-strain model of each cross-section (Fig. 4) to qualitatively reconstruct the fault geometry that may have caused the surface deformation around the Nopolo structure.

Fig. 12a shows the vertical surface displacements resulting from a unit stress drop along a listric fault. The fault tip is buried 1 km below the earth's surface and dips 66°. The fault dip decreases monotonically at 1 km increments to a sole-out depth of 5 km. The surface deflection is vertically exaggerated in the figure and forms a monocline above the tip of the buried fault. The maximum amplitude of the monocline is at the center of the fault and decreases elliptically towards the ends of the fault (Fig. 12a). Because we use an arbitrary stress drop along the listric fault, the magnitude of the vertical displacements scales linearly with total stress drop and fault slip. The surface displacements portrayed in Fig. 12a reflect the total displacement after 1×10^7 MPa of total stress release along the fault, whereas those in Fig. 12b reflect the deflection after 1×10^6 MPa of stress release.

To simulate the breaching of the monocline, we considered the displacement field that results from a listric normal fault that reaches the surface in Fig. 12b. Here, the fault dip at the surface is 72° and decreases monotonically to a depth of 5 km. The vertical surface displacements in the footwall of the listric normal fault are negligible compared with a blind listric normal fault and the case of a planar normal fault that breaches the surface (e.g. Willemse, 1997). As with the blind normal fault, the maximum surface displacement is at the center of the listric normal fault and decreases towards its ends.

6. Evolution of the Nopolo structure

The Nopolo structure is fundamentally the result of upward and lateral fault propagation based on lateral changes in structural style and geometry and inferences from our modeling. We divide the evolution of the structure into two phases; (1) monoclinal folding that produced 300–370 m of structural relief and (2) breaching of the monocline that produced offsets of 20–30 m.

6.1. Monoclinal stage

The results of our modeling and field observations suggest that the Nopolo structure initially formed by the upward propagation of two blind, steeply east-dipping, listric normal faults during the late Miocene. At the surface, the blind normal faults were manifest as two broad, east-facing monoclines above the normal faults (Fig. 13a). Along-strike variations in fault displacement and the depth

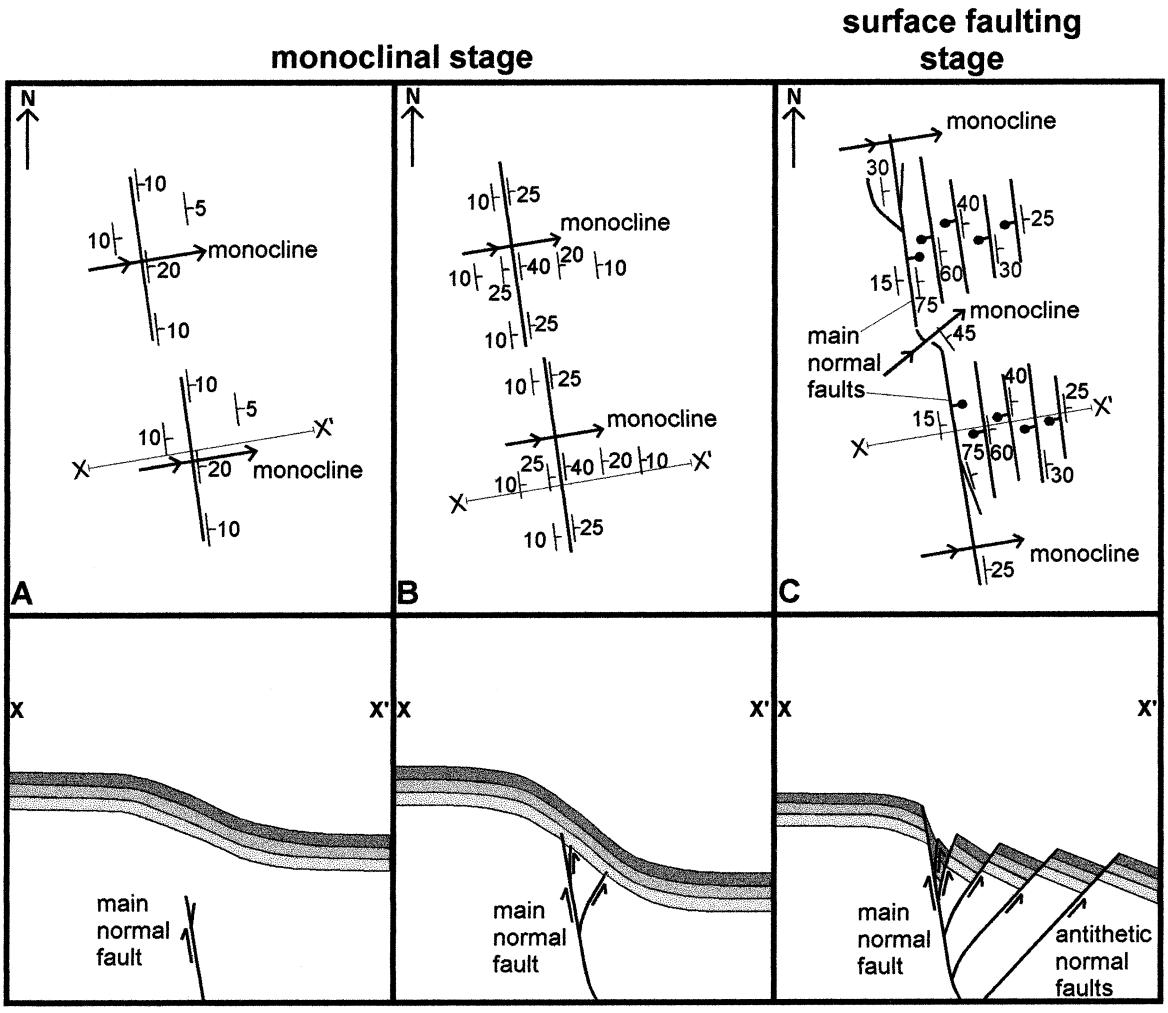

Fig. 13. Proposed evolution of the Nopolo structure shown in map view (top) and in profile (bottom). The three layers of strata are hypothetical and used to illustrate changes in geometry. (a) Two broad, gentle monoclines develop above blind, propagating normal faults. (b) As faults approach surface, monoclines steepen and become longer. (c) Faults breach the surface and offset the monoclines. Antithetic normal faults splay into hanging wall and offset strata. Footwall strata retain original monocline character, whereas hanging wall strata steepen near the main normal fault.

of the fault tip controlled the systematic changes in the dip of the limbs of the monoclines. Steeper dips (20–30°) were located near the midpoint of the faults where the fault tip was shallower and lesser dips (10–15°) were located near the ends of the faults where the fault tip was deeper (Fig. 13a). Based on estimates from the southern monocline (cross-section D–D′, Fig. 4), the formation of these early monoclines probably produced at least ~350 m of structural relief.

As the normal faults continued to propagate towards the surface, the buried sedimentary rocks of the lower Comondú Group were cut by the faults near the center of the monoclines (Fig. 13b). The exposure of the northern end of the southern monocline indicates that the limbs probably became as steep as ~40° prior to the onset of surface faulting. Our modeling results suggest that the normal fault was ~1 km below the surface at this time. Lateral variations in fault displacement had a profound effect on the steepness of monocline limbs. Near the midpoint of the faults, monocline limbs dip steeply where the fault tip is shallow. In contrast, near the ends of the fault, the limbs of the monoclines dip gently where the fault tip is deeper. Secondary faults may have developed at this point and probably consisted of steep antithetic and synthetic normal faults that splayed upward into the hanging wall region (Withjack et al., 1990).

6.2. Surface faulting stage

Once the main normal faults reached the surface, gently dipping footwall strata ceased to be folded and were preserved or may have rebounded slightly along the faults. The main normal faults lengthened and locally developed splays near their ends as lateral propagation continued (Fig. 13c). Stratigraphic offset, limited along the main normal faults (~20–30 m; Fig. 4), was more pronounced (>100 m) along west-dipping antithetic normal faults that became more numerous and longer as extension continued

(Fig. 13c). Steep secondary synthetic and antithetic normal faults dissected the limb of the monocline into discrete fault-bounded packages. These were rotated to steep orientations with the steepest strata in narrow grabens between the main normal faults and antithetic normal faults in the hanging wall (Fig. 13c). Strata bound by antithetic normal faults dip ~80–40° in the first 0.5 km east of the main normal fault and dip ~30–20° more than 0.5 km east of the main normal fault (Fig. 13c). These antithetic normal faults probably extend eastward at least ~6 km and bound 30–20° east-dipping packages of strata. Additionally, the northern and southern faulted monoclines may have linked as they propagated towards each other across the central monocline (Fig. 13c). Localized drag along normal faults may also have played a minor role in accentuating the dip of hanging wall strata near the faults. Steep east-dipping bedding in the northern fault zone domain near the main normal faults may be a product of monoclinal folding and fault drag (Fig. 3a).

7. Discussion

Many of the general characteristics and features of the Nopolo structure are consistent with previous studies from other extensional regions and from other experimental model results. Extensional monoclines and faulted monoclines along the eastern margin of the Gulf of Suez are strikingly similar to the Nopolo structure (e.g. Moustafa, 1993; Gawthorpe et al., 1997; Gupta et al., 1999; Sharp et al., 2000). However, the main normal faults have several kilometers of offset and have developed more fully than the Nopolo structure (Gawthorpe et al., 1997; Sharp et al., 2000).

The Nopolo structure contains several features that are consistent with observations made in experimental models. Withjack et al. (1990) showed that growth monoclines develop above the tips of propagating normal faults. Their results demonstrated that the dip of the underlying fault determines the steepness of the fold limb, the width of the fold, and the width of the deforming zone above the propagating fault tip. Steep (75°) faults have narrow folds with ~25° limb dips and narrow zones of deformation (similar to the Nopolo structure), whereas less steep faults (45°) have wide folds with ~15° limb dips and wide zones of deformation. Our modeling suggests that fault dip may have a similar, but more subtle effect.

Couples et al. (1994) showed that well-defined grabens develop in the hanging wall of faulted monoclines. These grabens are common throughout the Nopolo structure and are bounded by the main and antithetic normal faults. The results of Patton et al. (1998) also show steeply dipping hanging wall strata juxtaposed against the main fault, a persistent feature of the Nopolo structure.

Hardy and McClay (1999) presented a 2D kinematic model for extensional fault-propagation folds where the style and location of deformation hinged on the fault propagation-to-slip (p/s) ratio and the apical angle of the trishear region above the fault tip. Their results suggest that small apical angles produce steep monoclines with a more intense and narrow zone of deformation and tight folds adjacent to the master fault, similar to the Nopolo structure. The results of variable p/s ratios are not compatible with observations and inferences made for the Nopolo structure. Based on the width of the zone of deformation, the Nopolo structure probably initially developed a narrow monocline, suggesting a high p/s ratio. However, surface faulting is thought to have occurred late in the evolution of the Nopolo structure following a protracted period of fault-propagation folding and is suggestive of a low p/s ratio.

Withjack and Callaway (2000) demonstrated that the presence of a viscous layer, such as salt, promotes the formation of extensional monoclines. Their model results also show that low displacement rates and thin, strong overlying strata favor the development of broad monoclines. These results generally agree with our observations of the Nopolo structure. Although there are no viscous layers within the Nopolo structure, the overlying strata is relatively thin and cohesive, and displacement likely occurred at a much slower rate than other parts of the Loreto rift segment where monoclines are absent.

The formation of an extensional monocline prior to surface faulting appears common throughout the segment-bounding structures of the Loreto rift segment. The northern monocline (Fig. 2b) shows no evidence for surface faulting and therefore represents an extensional monocline where the normal fault is still blind. The Escondido fault is located south of the Nopolo structure (Fig. 2b) and may be a more evolved form of the Nopolo structure because it has ~2 km of structural relief. The Nopolo structure captures the geometry of an extensional monocline that has been slightly breached by a propagating normal fault. It is likely that surface faulting on the Nopolo structure ceased soon after the monocline was breached, as the regional extension direction changed at ~5–6 Ma and the dextral-normal Loreto fault to the north began to accommodate much of the regional strain.

Acknowledgements

This work was supported by NSF grants EAR-9526505 and EAR-9802792 (Umhoefer), GSA student research grant 6359-98 (Willsey), an ARCO Field Research Grant (Willsey) and a Northern Arizona University Friday Lunch Clubbe grant (Willsey). We thank Jason Hooten, Erika Willsey, and Mike Puchalski for field assistance during the winter of 1999, Becky Dorsey and Larry Mayer for discussions of the structure of other parts of the Loreto region and initial work on the Nopolo structure, and Susanne Janecke, Rolf Ackermann, and Special Editor Ted Apotria for thorough reviews of the manuscript.

References

Allmendinger, R.W., Marrett, R.A., Cladauhos, T., 1989. Faultkin computer program, version 3.8a.

Axen, G., 1995. Extensional segmentation of the Main Gulf Escarpment, Mexico and United States. Geology 23, 515–518.

Chester, J.S., Spang, J.H., Logan, J.M., 1988. Comparison of thrust fault models to basement-cored folds in the Rocky Mountain foreland. In: Schmidt, C.J., Perry, W.J. (Eds.). Interaction of the Rocky Mountain Foreland and the Cordilleran Thrust Belt. Geological Society of America Memoir 171, pp. 65–74.

Clark, S.P.J., 1966. Handbook of Physical Constants. Geological Society of America, Boulder, CO.

Cooke, M.L., 1996. Frictional slip and fractures associated with faults and folds. Ph.D. thesis, Stanford University.

Couples, G.D., Lewis, H., 1998. Lateral variations of strain in experimental forced folds. Tectonophysics 295, 79–91.

Couples, G.D., Stearns, D.W., Handin, J.W., 1994. Kinematics of experimental forced folds and their relevance to cross-section balancing. Tectonophysics 233, 193–213.

Crouch, S.L., Starfield, A.M., 1983. Boundary Element Methods in Solid Mechanics. George Allen and Unwin, London.

Davis, G.H., 1978. Monocline fold pattern of the Colorado Plateau. In: Matthews, V. (Ed.). Laramide Folding Associated with Basement Block Faulting in the Western United States. Geological Society of America Memoir 151, pp. 215–233.

Davis, G.H., 1999. Structural geology of the Colorado Plateau region of southern Utah. Geological Society of America Special Paper, 342.

DeMets, C., 1995. A reappraisal of seafloor spreading lineations in the Gulf of California: implications for the transfer of Baja California to the Pacific plate and estimates of Pacific–North America motion. Geophysical Research Letters 22, 3545–3548.

Dorsey, R.J., Umhoefer, P.J., 2000. Tectonic and eustatic controls on sequence stratigraphy of the Pliocene Loreto basin, Baja California Sur, Mexico. Geological Society of America Bulletin 112, 177–199.

Friedman, M., Hugman, R.H.H., Handin, J., 1980. Experimental folding of rocks under confining pressure. Part VIII — forced folding of unconsolidated sand and lubricated layers of limestone and sandstone. Geological Society of America Bulletin 91, 307–312.

Gardner, J.N., Lavine, A., WoldeGabriel, G., Krier, D., Vaniman, D., Caporuscio, F., Lewis, C., Reneau, P., Kluk, E., Snow, M.J., 1999. Structural geology of the northwestern portion of Los Alamos National Laboratory, Rio Grande rift, New Mexico: implications for seismic surface rupture potential from TA-3 to TA-55. Los Alamos National Laboratory Report LA-13589-MS.

Gawthorpe, R.L., Sharp, I., Underhill, J.R., Gupta, S., 1997. Linked sequence stratigraphic and structural evolution of propagating normal faults. Geology 25, 795–798.

Gross, M.R., Becker, A., Gutiérrez-Alonso, G., 1997. Transfer of displacement from multiple slip zones to a major detachment in an extensional regime: example from the Dead Sea rift, Israel. Geological Society of America Bulletin 109, 1021–1035.

Gupta, S., Underhill, J.R., Sharp, I.R., Gawthorpe, R.L., 1999. Role of fault interactions in controlling synrift sediment dispersal patterns: Miocene, Abu Alaqa Group, Suez Rift, Sinai, Egypt. Basin Research 11, 167–189.

Hancock, P.L., Barka, A.A., 1987. Kinematic indicators on active normal faults in western Turkey. Journal of Structural Geology 9, 573–584.

Hardy, S., McClay, K., 1999. Kinematic modeling of extensional fault-propagation folding. Journal of Structural Geology 21, 695–702.

Hausback, B.P., 1984. Cenozoic volcanic and tectonic evolution of Baja California, Mexico. In: Frizzell, V.A. (Ed.). Geology of the Baja California Peninsula. Society of Economic Paleontologists and Mineralogists, Pacific Section, pp. 219–236.

Henry, C.D., 1989. Late Cenozoic Basin and Range structure in western Mexico adjacent to the Gulf of California. Geological Society of America Bulletin 101, 1147–1156.

Jaeger, J.C., Cook, N.G.W., 1976. Fundamentals of Rock Mechanics. Chapman and Hall, London.

Janecke, S., Vandenburg, C.J., Blankenau, J.J., 1998. Geometry, mechanisms, and significance of extensional folds from examples in the Rocky Mountain Basin and Range province, U.S.A. Journal of Structural Geology 20, 841–856.

Karig, D.E., Jensky, W., 1972. The proto-gulf of California. Earth and Planetary Science Letters 17, 169–174.

Krantz, R., 1989. Laramide structures of Arizona. In: Jenney, J.P., Reynolds, S.J. (Eds.). Geologic Evolution of Arizona. Arizona Geological Society Digest 17, pp. 463–483.

Lonsdale, P., 1989. Geology and tectonic history of the Gulf of California. In: Winterer, E.L. (Ed.). The Eastern Pacific Ocean and Hawaii. Geological Society of America, pp. 499–521.

Marrett, R., Allmendinger, R.W., 1990. Kinematic analysis of fault-slip data. Journal of Structural Geology 12, 973–986.

Mayer, L., Vincent, K.R., 1999. Active tectonics of the Loreto area, Baja California Sur, Mexico. Geomorphology 27, 243–255.

McLean, H., 1988. Reconnaissance geologic map of the Loreto and part of the San Javier quadrangles, Baja California Sur, Mexico. U.S. Geological Survey Map MF-2000, scale 1:50,000.

Mitra, S., 1993. Geometry and kinematic evolution of inversion structures. American Association of Petroleum Geologists Bulletin 77, 1159–1191.

Moustafa, A.M., 1993. Structural chracteristics and tectonic evolution of the east-margin blocks of the Suez rift. Tectonophysics 223, 381–399.

Patton, T.L., Logan, J.M., Friedman, M., 1998. Experimentally generated normal faults in single-layer and multilayer limestone specimens at confining pressure. Tectonophysics 295, 53–77.

Petit, J.P., 1987. Criteria for sense of movement on fault surfaces in brittle rocks. Journal of Structural Geology 9, 597–608.

Reches, Z., 1978. Development of monoclines: Part I. Structure of the Palisades Creek branch of the East Kaibab monocline, Grand Canyon, Arizona. In: Matthews, V. (Ed.). Laramide Folding Associated with Basement Block Faulting in the Western United States. Geological Society of America Memoir 151, pp. 235–272.

Schlische, R.W., 1995. Geometry and origin of fault-related folds in extensional settings. American Association of Petroleum Geologists Bulletin 79, 1661–1678.

Segall, P., Pollard, D.D., 1980. The mechanics of discontinuous faults. Journal of Geophysical Research 85, 4337–4350.

Sharp, I.R., Gawthorpe, R.L., Underhill, J.R., Gupta, S., 2000. Fault-propagation folding in extensional settings: examples of structural style and synrift sedimentary responses from the Suez Rift, Sinai, Egypt. Geological Society of America Bulletin 112, 1877–1899.

Smith, J.V., Durney, D.W., 1992. Experimental formation of brittle structural assemblages in oblique divergence. Tectonophysics 216, 235–253.

Stock, J.M., Hodges, K.V., 1989. Pre-Pliocene extension around the Gulf of California and the transfer of Baja California to the Pacific plate. Tectonics 8, 99–115.

Stock, J.M., Lee, J., 1994. Do microplates in subduction zones leave a geological record? Tectonics 13, 1472–1487.

Thomas, A.L., 1993. Poly3D: a three-dimensional, polygonal element, displacement discontinuity boundary element computer program with applications to fractures, faults, and cavities in the Earth's crust. M.S. thesis, Stanford University.

Tindall, S.E., Davis, G.H., 1999. Monocline development by oblique-slip fault-propagation folding: the east Kaibab monocline, Colorado Plateau, Utah. Journal of Structural Geology 21, 1303–1320.

Tron, V., Brun, J., 1991. Experiments on oblique rifting in brittle-ductile systems. Tectonophysics 188, 71–84.

Umhoefer, P.J., Stone, K.A., 1996. Description and kinematics of the SE Loreto basin fault array, Baja California Sur, Mexico: a positive field test of oblique-rift models. Journal of Structural Geology 18, 595–614.

Umhoefer, P.J., Mayer, L., Dorsey, R.J., 1997. Rift segmentation on the margin of the Gulf of California near Loreto, Baja California peninsula, Mexico. Geological Society of America Abstracts with Programs 29, 481.

Umhoefer, P.J., Dorsey, R.J., Willsey, S., Mayer, L., Renne, P., 2001a. Stratigraphy and geochronology of the Comondú Group near Loreto, Baja California Sur, Mexico. Sedimentary Geology, in press.

Umhoefer, P.J., Mayer, L., Dorsey, R.J., 2001b. Evolution of the margin of the Gulf of California near Loreto, Baja California peninsula, Mexico. Geological Society of America Bulletin, in review.

Walsh, J.J., Watterson, J., 1987. Distribution of cumulative displacement and seismic slip on a single normal fault surface. Journal of Structural Geology 9, 1039–1046.

Willemse, E.J.M., 1997. Segmented normal faults: correspondence between three-dimensional mechanical models and field data. Journal of Geophysical Research 102, 675–692.

Withjack, M.O., Olson, J., Peterson, E., 1990. Experimental models of extensional forced folds. American Association of Petroleum Geologists Bulletin 74, 1038–1054.

Withjack, M.O., Callaway, S., 2000. Active normal faulting beneath a salt layer: an experimental study of deformation patterns in the cover sequence. American Association of Petroleum Geologists Bulletin 84, 627–651.

Zanchi, A., 1994. The opening of the Gulf of California near Loreto, Baja California, Mexico: from basin and range extension to transtensional tectonics. Journal of Structural Geology 16, 1619–1639.